Photoelectron imaging spectroscopy of Ag_3^- in the S_0 and S_1 states

Suzuki, Yuta
Department of Chemistry, Faculty of Science, Kyushu University

Nishizato, Tasuku
Department of Chemistry, Faculty of Science, Kyushu University

Matsumoto, Kazuaki
Department of Chemistry, Faculty of Science, Kyushu University

Ushiki, Yuta
Department of Chemistry, Faculty of Science, Kyushu University

他

https://hdl.handle.net/2324/7420557

出版情報：The Journal of Chemical Physics. 162 (18), pp.184304-, 2025-05-12. AIP Publishing
バージョン：

Photoelectron imaging spectroscopy of Ag_3^- in the S_0 and S_1 states

Yuta Suzuki, Tasuku Nishizato, Kazuaki Matsumoto, Yuta Ushiki, Yuma Aoki,
Akira Terasaki,[a)] and Takuya Horio[a)]

Department of Chemistry, Faculty of Science, Kyushu University, 744 Motooka, Nishi-ku, Fukuoka 819-0395, Japan

We explore laboratory-frame photoelectron angular distributions (LF-PADs) originating from the outermost two orbitals, σ_u (the highest occupied molecular orbital: HOMO) and σ_g (HOMO−1), of the silver trimer anion (Ag_3^-) in the $S_0(^1\Sigma_g^+)$ state. The experiment was performed by our novel photoelectron imaging technique using a high-repetition-rate tunable laser [T. Horio *et al.*, J. Chem. Phys. **162**, 026101 (2025)]. The LF-PAD for σ_u is found to be highly energy-dependent in a photoelectron kinetic energy (PKE) range from 0 to 1.57 eV; an isotropic LF-PAD with an anisotropy parameter $\beta \sim 0$ is observed at the detachment threshold, exemplifying the Wigner threshold law, whereas β value decreases down to $\beta = -0.4$ at 0.46 eV, followed by an increase up to $\beta = 0.6$ at 1.57 eV, as PKE increases. A small dip discernible in the PKE range of 1.2 – 1.3 eV suggests an influence of the autodetachment process on the β value, which is via bound electronic state(s) embedded in the $D_0(^2\Sigma_u^+) + e^-$ continuum. On the other hand, the LF-PAD for σ_g exhibits a strong anisotropy parallel to the laser polarization with β of ~1 in 0 – 0.39 eV. These contrasted trends are qualitatively reproduced by theoretical modeling of LF-PAD that accounts for photoelectron partial waves allowed for each photodetachment process. Furthermore, two-photon detachment spectra via the excited $S_1(^1\Sigma_u^+)$ state are presented, where the relative band intensities for the two detachment channels, $D_0(^2\Sigma_u^+) + e^- \leftarrow S_1(^1\Sigma_u^+)$ and $D_1(^2\Sigma_g^+) + e^- \leftarrow S_1(^1\Sigma_u^+)$, are discussed in terms of their leading electronic configurations.

[a)]Authors to whom correspondence should be addressed. Electronic mail: horio@chem.kyushu-univ.jp, terasaki@chem.kyushu-univ.jp

I. INTRODUCTION

The silver trimer anion, Ag_3^-, has been receiving continuous attention over the past decades. A simple Hückel model[1–3] and *ab initio* calculations[4] predicted that the equilibrium geometry of Ag_3^- in the ground electronic state is linear, i.e., $S_0(^1\Sigma_g^+)$, where four valence electrons including the excess charge occupy the outermost molecular orbitals (MOs), σ_u (the highest occupied MO: HOMO) and σ_g (HOMO−1), created mainly by Ag 5s orbitals. The high-resolution photodetachment spectroscopy by Lineberger and coworkers[5] found that the $D_0(^2\Sigma_u^+) + e^- \leftarrow S_0(^1\Sigma_g^+)$ transition (i.e., the detachment of an electron from HOMO) occurs at 2.43 ± 0.01 eV, which corresponds to the vertical detachment energy (VDE). At the same time, Ganteför et al.[6] reported a VDE value of 2.452 eV using zero-kinetic-energy-electron (ZEKE) spectroscopy of jet-cooled Ag_3^-; the authors pointed out that the slightly larger VDE is likely due to the internal temperature of the samples lower than that in ref. [5]. A theoretical estimate of 2.455 eV by Bonačić-Koutecký et al.[4] is in excellent agreement with these experimental VDEs. The electron binding energy for the $D_1(^2\Sigma_g^+) + e^- \leftarrow S_0(^1\Sigma_g^+)$ transition (i.e., the detachment of an electron from HOMO−1) has been reported to be 3.62 eV by Handschuh et al.[7] This anion also served as a precursor for demonstrating negative-to-neutral-to-positive (NeNePo) spectroscopy that explores time-resolved dynamics in the neutral state.[8,9]

Recently, we conducted photodestruction action spectroscopy of Ag_3^- in the photon energy range of 2 – 5 eV using an ion trap to investigate its excited electronic states,[10] where photodestruction signals (i.e., depletion in the number of Ag_3^- anions in the trap) were obtained through detachment of the excess electron and/or fragmentation of Ag_3^- upon photoirradiation. It was found that the spectrum exhibits a relatively sharp resonance due to the $S_1(^1\Sigma_u^+) \leftarrow S_0(^1\Sigma_g^+)$ transition at 2.39 eV, i.e., just below VDE, which is followed by a broad hump around 3.8 eV.

These studies have motivated us to further advance the continuous investigations on Ag_3^-. The objective of the present study is twofold. First, we attempt to characterize HOMO (σ_u) and HOMO−1 (σ_g) of Ag_3^- in $S_0(^1\Sigma_g^+)$ from energy-dependent laboratory-frame photoelectron angular distributions

(LF-PADs). To this end, we employ our novel photoelectron velocity-map imaging (VMI) setup that utilizes a tunable femtosecond (fs) laser at a 100 kHz repetition rate. The technique was demonstrated very recently by measuring two-dimensional (2D) projections of photoelectrons detached from Ag_3^- at various photon energies.[11] Here, we provide a full account of the observed images along with a theoretical modeling of LF-PAD using the ezDyson program.[12,13] Second, taking advantage of tunable and short pulses from the 100-kHz laser system, we attempt to obtain one-color, two-photon detachment spectra via the $S_1(^1\Sigma_u^+)$ state of Ag_3^- to gain insight into the electronic configuration of this transient state.

II. EXPERIMENTAL AND COMPUTATIONAL METHODS

The whole experimental setup including the photodetachment light source has been described in our recent reports.[11,14] A continuous beam of Ag_3^- was produced by combination of a magnetron-sputtering ion source and a quadrupole mass filter (QMF). The Ag_3^- anions were delivered from the exit lens of QMF to a potential switch (PS) with octopole ion guides driven by radio-frequency (rf) generators operated at a frequency of ~1 MHz. At the PS, the continuous beam of Ag_3^- was chopped into 100-kHz anion bunches by +0.4-kV pulses synchronized with laser pulses from an Yb:KGW (ytterbium-doped potassium gadolinium tungstate) regenerative amplifier. The light source produced ~210 fs, 100 μJ, and 1030 nm pulses with linear polarization at a 100 kHz repetition rate; 80% of its output (i.e., 80 μJ/pulse) was used to pump an optical parametric amplifier that generated fs pulses tunable from near infrared (NIR) to visible (VIS) (620 – 2600 nm). For generating wavelengths shorter than 620 nm, we used an additional beta-barium borate (β-BBO) crystal for frequency doubling the NIR and VIS pulses.

The bunched Ag_3^- beam focused with an einzel lens was admitted to an assembly of photoelectron extraction lenses optimized at low extraction fields[15] for achieving the VMI condition.[16] For examining LF-PADs, we measured two-dimensional (2D) projections of photoelectrons ejected by the fs pulses into three dimension. The photon energy was varied from 2.43 to 4.00 eV to observe one-photon detachment from HOMO (σ_u) and HOMO−1 (σ_g) of Ag_3^- in $S_0(^1\Sigma_g^+)$, whereas it was tuned at the resonance to the $S_1(^1\Sigma_u^+) \leftarrow S_0(^1\Sigma_g^+)$ transition in one-color, two-photon detachment experiments. The peak laser power at the laser-anion interaction region was estimated to be $10^8 - 10^9$ W/cm^2.

A dual microchannel plate (ϕ40 mm) coupled with a phosphor screen (P43) was used to visualize photoelectron 2D projections. In our previous studies,[11,14,17,18] we used a frame-based (i.e., conventional) digital camera for obtaining photoelectron images, where intensities of bright spots on the phosphor screen were recorded for 500 ms and the measurements were repeated until an accumulated image reached an acceptable signal to noise ratio. In the present study, we have installed a new digital camera (SilkyEvCam HD, 1280×720 pixels, CenturyArks Co., Ltd.) equipped with an event-based vision sensor, which enables us to perform event counting of bright spots on the phosphor screen (see Supplementary Information for further details). Since some of the bunched Ag_3^- anions emitted low energy electrons upon collision with the VMI electrodes, an image of such background electrons was recorded with the photodetachment laser turned off (a laser-off image), which was subtracted from a laser-on image to remove the backgrounds. The 2D projection thus obtained was analyzed by the polar onion-peeling (POP) method[19] to reconstruct the original 3D distribution of the detached photoelectrons, which yielded photoelectron-kinetic-energy (PKE) distributions (i.e., photoelectron spectra) and LF-PADs.

The electronic-structure calculations were performed with the Q-chem 5.4 package[20] to simulate energy dependence of LF-PADs using ezDyson 5.0.[12,13] The equilibrium geometry of Ag_3^- in the $S_0(^1\Sigma_g^+)$ state was optimized by the coupled-cluster single and double (CCSD) theory with the aug-cc-pVDZ-PP[21,22] basis set, which has found that the most stable structure is linear with the Ag–Ag bond lengths of 2.67 Å. The equation-of-motion ionization potential CCSD (EOM-IP-CCSD) methodology with the same basis set was further performed to calculate Dyson orbitals, which were used for ezDyson to simulate LF-PADs. For comparison, we also calculated LF-PAD using Kohn–Sham orbitals with BP86[23,24] functional and LanL2DZ[25] basis set with the corresponding effective core potential. EOM-EE-

CCSD theory calculations were also used to estimate vertical electron excitation energies (VEEs) of optically allowed transitions from the gerade state of $S_0(^1\Sigma_g^+)$ to ungerade states.

III. RESULTS AND DISCUSSION

A. Energy dependence of LF-PADs from σ_u and σ_g orbitals

Figure 1 shows 2D slice images of photoelectrons detached from Ag_3^- in the $S_0(^1\Sigma_g^+)$ state, obtained for the photon energies of (a) 2.43, (b) 2.53, (c) 2.64, (d) 2.76, (e) 2.89, (f) 3.02, (g) 3.18, (h) 3.35, (i) 3.45, (j) 3.65, (k) 3.77, and (l) 3.88 eV; the original projected images before transformed to these 2D slices are shown in Fig. S3 in Supplementary Material. Isotropic distributions are observed at (a) 2.43 and (b) 2.53 eV. The images gradually become anisotropic with more photoelectrons emitted perpendicular to the laser polarization direction (ε in Fig. 1(a)) with increasing the photon energy from (c) 2.64 to (e) 2.89 eV; the ring diameter increases accordingly, which is proportional to the photoelectron velocity. The perpendicular anisotropy turns to be less prominent at (f) 3.02 eV. Then the LF-PADs return to be nearly isotropic at (g) 3.18, (h) 3.35, and (i) 3.45 eV. These photoelectrons

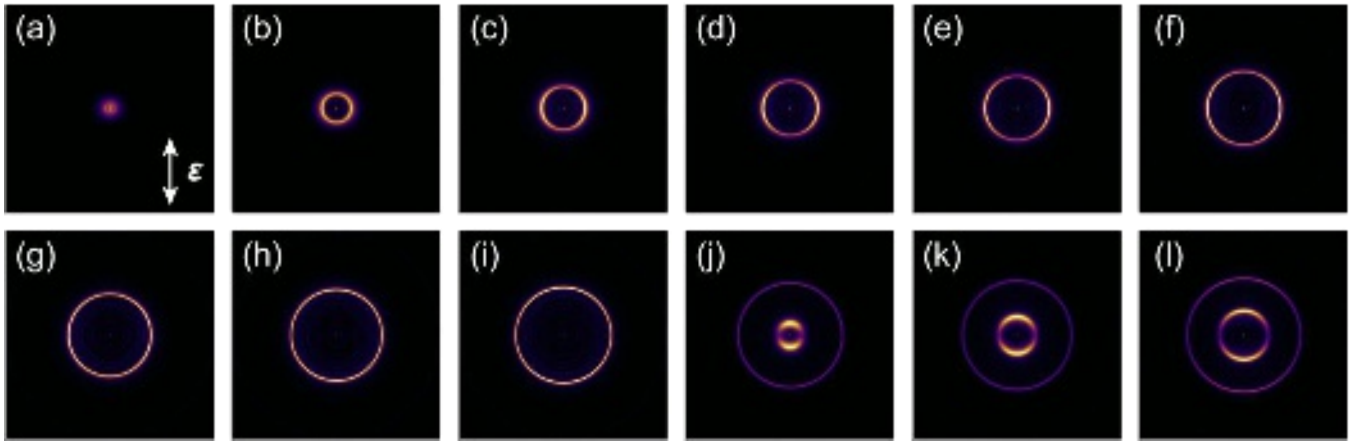

Figure 1. 2D slices of photoelectron distributions for Ag_3^- obtained at (a) 2.43, (b) 2.53, (c) 2.64, (d) 2.76, (e) 2.89, (f) 3.02, (g) 3.18, (h) 3.35, (i) 3.45, (j) 3.65, (k) 3.77, and (l) 3.88 eV. The direction of the polarization vector, ε, of the photodetachment laser is indicated by a double arrow in (a). The original projected images before transformation to these 2D slices can be found in Fig. S3 in Supplementary Information.

originate from the lowest-energy detachment channel, $D_0(^2\Sigma_u^+) + e^- \leftarrow S_0(^1\Sigma_g^+)$. The image indicates a significant change at (j) 3.65 eV, showing an additional component at the center. The inner component is assignable to the second detachment channel, $D_1(^2\Sigma_g^+) + e^- \leftarrow S_0(^1\Sigma_g^+)$. As manifested in Figs. 1(j), 1(k), and 1(l), the photoelectrons for this channel exhibit a strong anisotropy parallel to ε.

In single-photon detachment from randomly oriented samples with a linearly-polarized light, LF-PAD is proportional to $1 + \beta P_2(\cos\theta)$,[26] where θ, β, and $P_2(x)$ are the polar angle with respect to the laser polarization vector (ε), the photoelectron anisotropy parameter ranging from −1 to +2, and the 2nd order Legendre polynomial, respectively. The β parameters obtained by POP are plotted in Fig. 2(a) as a function of PKE for the photoelectrons both in the $D_0(^2\Sigma_u^+) + e^- \leftarrow S_0(^1\Sigma_g^+)$ (circles) and in the $D_1(^2\Sigma_g^+) + e^- \leftarrow S_0(^1\Sigma_g^+)$ transitions (squares). The β values for the former transition vary significantly from negative through positive as a function of PKE, whereas those for the latter transition are less energy-dependent, although the data points are limited; the estimation of errors in the β parameters is described in Supplementary Material.

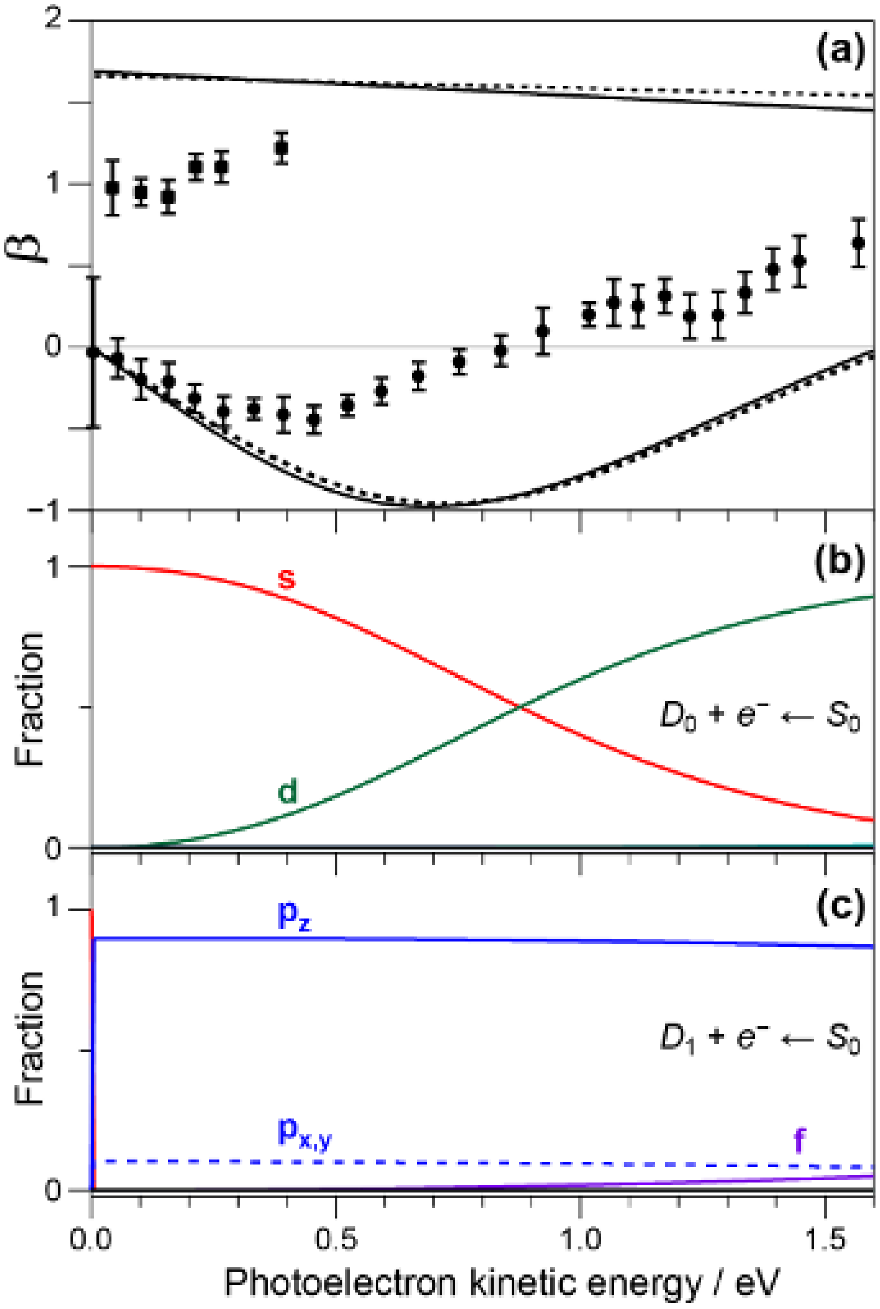

Figure 2. (a) Photoelectron anisotropy parameters, *β*, evaluated from the photoelectron images for the $D_0(^2\Sigma_u^+) + e^- \leftarrow S_0(^1\Sigma_g^+)$ (circles) and $D_1(^2\Sigma_g^+) + e^- \leftarrow S_0(^1\Sigma_g^+)$ transitions (squares) of Ag_3^- as a function of photoelectron kinetic energy. The results of simulation are superimposed by the solid and dashed curves, which are obtained by ezDyson 5.0 using EOM-IP-CCSD/aug-cc-pVDZ-PP and BP86/LanL2DZ level of calculations, respectively (see the text). (b) and (c): Partial wave analyses for photoelectrons ejected via the $D_0(^2\Sigma_u^+) + e^- \leftarrow S_0(^1\Sigma_g^+)$ and the $D_1(^2\Sigma_g^+) + e^- \leftarrow S_0(^1\Sigma_g^+)$ transitions, respectively, obtained by the EOM-IP-CCSD/aug-cc-pVDZ-PP level of calculations.

132

The EOM-IP-CCSD theory calculation with aug-cc-pVDZ-PP basis sets performed in the present study has found that the former and the latter transitions can be well described by detachment of an electron from the outermost two MOs, σ_u and σ_g, respectively. The corresponding valence electron configurations of $D_0(^2\Sigma_u^+)$ and $D_1(^2\Sigma_g^+)$ are therefore approximated as $(\sigma_g)^2(\sigma_u)^1$ and $(\sigma_g)^1(\sigma_u)^2$, as illustrated in Fig. 3. The calculation also evaluated the VDE and the second electron binding energy to be 2.33 and 3.59 eV, respectively, which reasonably reproduce the experimental values of 2.43 (ref. [5]) / 2.452 (ref. [6]) and 3.62 eV.[7]

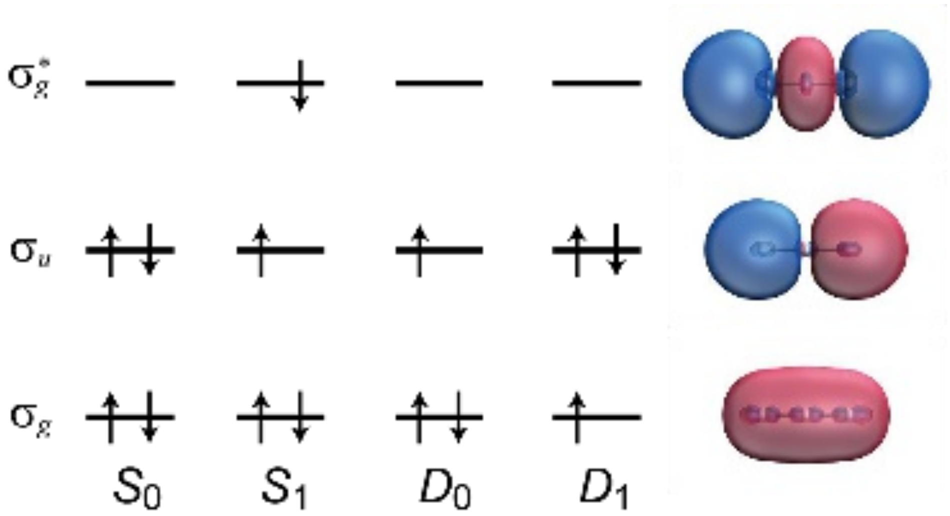

Figure 3. The leading electronic configurations of S_0, S_1, D_0, and D_1 states for anionic and neutral silver trimers along with the iso-surface plots of σ_g, σ_u, and σ_g^* MOs formed mainly with 5s atomic orbitals of silver atoms. The plots were obtained by the BP86/LanL2DZ level of calculation.

Due to its ungerade symmetry, single-photon detachment from the σ_u orbital results in emission of photoelectron partial waves only with gerade symmetries (i.e., s, d, g, …). According to the Wigner threshold law,[27] the photodetachment cross section is proportional to $E^{l+1/2}$, where E and l denote PKE and the angular momentum quantum number of the detached electron, respectively. This indicates that s-wave ($l = 0$) is dominant when E is close to zero, leading to $\beta = 0$. As manifested in Fig. 2(a), our experimental result obtained for the photodetachment from the σ_u orbital (i.e., $D_0(^2\Sigma_u^+) + e^- \leftarrow S_0(^1\Sigma_g^+)$)

exemplifies this threshold law. On the other hand, photodetachment from the σ_g orbital gives rise to emission of photoelectron partial waves only with ungerade symmetries, (i.e., p, f, h, …), indicating that the β value does not fall off to zero even at the threshold, which is consistent with the present observation as far as PKE is greater than ~0.04 eV (the first data point for the $D_1(^2\Sigma_g^+) + e^- \leftarrow S_0(^1\Sigma_g^+)$ channel in Fig. 2(a)).

B. Theoretical modeling of LF-PADs by ezDyson

The solid and dashed curves in Fig. 2(a) present theoretical β parameters evaluated from LF-PADs obtained with the EOM-IP-CCSD/aug-cc-pVDZ-PP and BP86/LanL2DZ levels of calculations, respectively. As mentioned in Section II, the former level of calculation provided the Dyson orbitals for the $D_0(^2\Sigma_u^+) + e^- \leftarrow S_0(^1\Sigma_g^+)$ and $D_1(^2\Sigma_g^+) + e^- \leftarrow S_0(^1\Sigma_g^+)$ photodetachment processes, whereas the latter produced the Kohn–Sham orbitals shown in Fig. 3, which were used as substitutes for the corresponding Dyson orbitals; either Dyson or Kohn–Sham orbitals were used for the evaluation of β parameters. In both cases, we assumed a plane wave for the photoelectron wave function with the maximum angular momentum quantum number of 5 (i.e., h-wave). The trends in the energy dependence of the experimental β parameters are reproduced by both theoretical approaches qualitatively; the simulations either underestimate in the $D_0(^2\Sigma_u^+) + e^- \leftarrow S_0(^1\Sigma_g^+)$ channel or overestimate in the $D_1(^2\Sigma_g^+) + e^- \leftarrow S_0(^1\Sigma_g^+)$ channel.

Figure 2(b) shows partial wave decompositions for photoelectrons ejected from the $D_0(^2\Sigma_u^+) + e^- \leftarrow S_0(^1\Sigma_g^+)$ transition, as obtained by the EOM-IP-CCSD/aug-cc-pVDZ-PP level of calculation. It is obvious that s-wave (red curve) is dominant at the threshold, which reconfirms the Wigner threshold law. As PKE increases, the contribution of d-wave (green curve) shows up, which results in interference between s- and d-waves. In the plane-wave approximation, where interaction of an outgoing electron and a residual neutral core is ignored, the s- and d-waves exhibit destructive interference along the laser polarization axis.[28,29] This leads to negative β values (see the solid line in the lower part of Fig. 2(a)) from the threshold to around 0.7 eV with the minimum value of −1, followed by a monotonic increase, as the contribution of d-wave becomes dominant above 0.9 eV. Although this scenario qualitatively explains the energy dependence observed for the β values, the experimental data exhibit a minimum with $\beta = -0.4$ at 0.46 eV. The underestimation of β values in the ezDyson calculations is ascribed to the assumption that outgoing photoelectrons are described as a plane wave. Figure 2(c), on the other hand, shows similar partial wave decompositions for photoelectrons in the $D_1(^2\Sigma_g^+) + e^- \leftarrow S_0(^1\Sigma_g^+)$ transition. The leading contribution of p_z-wave in this channel, which is dominant even just above the threshold, explains the high β values ($\beta > 1$) as presented in the upper part of Fig. 2(a). The partial-wave decomposition analysis is thus qualitatively in line with the symmetry considerations discussed above.

C. Comparison with LF-PADs for Na_3^-

Herein, we compare our experimental results for Ag_3^- with those observed for Na_3^-. The equilibrium geometry of Na_3^- in the S_0 state is also linear with the bond lengths of 3.581 Å.[30] Therefore, the valence electron configuration is expected to be $(\sigma_g)^2(\sigma_u)^2$ as well, which are created by the interaction of Na 3s orbitals. Using an excimer-laser-pumped dye laser generating VIS and ultraviolet pulses with 1.64 – 4.28 eV photon energies, Bartels et al.[31] investigated Na_3^- by measuring energy-dependent LF-PADs for photodetachment from σ_u and σ_g orbitals. Due to the tuning range of the detachment laser with respect to the VDE of Na_3^- (1.158 ± 0.010 eV),[32] the minimum PKE of the measurement for the σ_u orbital was 0.48 eV, where isotropic distribution ($\beta \sim 0$) is observed. As PKE increases, the measured β value rises and reaches ~1.8 at PKE = 3.1 eV. Although the absolute values of β are different from those obtained for Ag_3^-, the upward trend in β values above ~0.5 eV is common to these two clusters. As for LF-PAD from the σ_g orbital, the β values obtained for Na_3^- are 1.2 – 1.3 in the PKE region of 0.0 – 0.4 eV,[31] which are comparable with those for Ag_3^-. Thus, the present study has shown that Na_3^- and Ag_3^- are valence iso-electronic systems in terms of the photoelectron angular anisotropy.

D. Excited states below and above the photodetachment threshold

Closer examination of Fig. 2(a) reveals a small dip in the experimental β values around 1.2 – 1.3 eV for the $D_0(^2\Sigma_u^+) + e^- \leftarrow S_0(^1\Sigma_g^+)$ channel (circles). To discuss this point, we refer to the photodestruction action spectrum of Ag_3^- in Fig. 4 (blue triangles) cited from ref.,[10] which was obtained using an ion trap cooled at 100 K. A sharp resonance signal is observed at 2.39 eV, just below VDE (the vertical dashed line in the figure), which is assignable to the $S_1(^1\Sigma_u^+) \leftarrow S_0(^1\Sigma_g^+)$ absorption; a tail extending toward a lower energy region is attributed to hot bands that are unresolved in our measurements;[10] the harmonic vibrational frequencies of the symmetric stretching, bending, and anti-symmetric stretching modes were

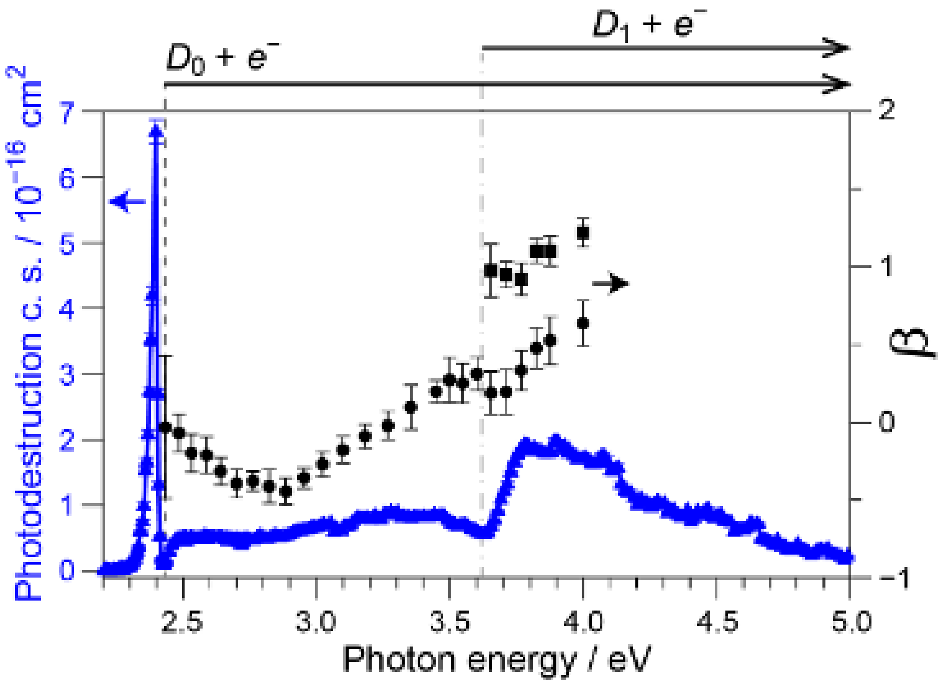

Figure 4. Photodestruction action spectra (blue triangles) of Ag_3^- obtained at an ion trap temperature of 100 K,[10] along with the β values for the $D_0(^2\Sigma_u^+) + e^- \leftarrow S_0(^1\Sigma_g^+)$ (circles) and $D_1(^2\Sigma_g^+) + e^- \leftarrow S_0(^1\Sigma_g^+)$ transitions (squares) plotted as a function of photon energy. The vertical dashed line shows the VDE, while the dash-dotted line indicates the second detachment threshold.

estimated to be 110, 39, and 179 cm^{-1}, respectively, by the CCSD/aug-cc-PVDZ-PP level of calculation. Such an asymmetric profile due to hot bands is seen also in the photodetachment spectra of Ag_3^- in ref. [5] and in the present study (see Fig. S5 in Supplementary Information).

We confirmed that the photodestruction signal corresponding to the $S_1(^1\Sigma_u^+) \leftarrow S_0(^1\Sigma_g^+)$ transition is induced by one-photon process. This sharp resonance is followed by nearly structureless absorption with its onset at the VDE. This manifests that the transition from $S_0(^1\Sigma_g^+)$ to the $D_0(^2\Sigma_u^+) + e^-$ continuum indeed starts around this energy, yielding the structureless absorption from the detachment threshold. Another feature discernible in the spectrum is a broad hump observed around 3.8 eV. As summarized in Table S2 in Supplementary Information, the present EOM-EE-CCSD/aug-cc-pVDZ-PP calculation predicts that optically allowed states lie at 2.45 ($^1\Sigma_u^+$), 3.23 ($^1\Pi_u$), 3.42 ($^1\Sigma_u^+$), 3.57 ($^1\Sigma_u^+$) , 4.01 ($^1\Pi_u$), and 4.97 ($^1\Pi_u$) eV. The lowest one corresponds reasonably to the $S_1(^1\Sigma_u^+)$ state. The photoabsorption from $S_0(^1\Sigma_g^+)$ to the $^1\Sigma_u^+$ state at 3.57 eV and/or the $^1\Pi_u$ state at 4.01 eV could account for the 3.8-eV hump, which slightly modifies our former assignment proposed in ref. [10]. Another broad band seen in 3.1 – 3.5 eV, which is rather unnoticeable most likely due to overlap of the $D_0(^2\Sigma_u^+) + e^- \leftarrow S_0(^1\Sigma_g^+)$ continuum absorption, may be a signature of two other states below 3.5 eV.

Here, we superimpose the experimental β values on the photodesctruction action spectrum, which are already presented in Fig. 2(a) but are replotted as a function of photon energy in Fig. 4. The result reveals that the variation of the β values associated with the $D_0(^2\Sigma_u^+) + e^- \leftarrow S_0(^1\Sigma_g^+)$ channel (circles in Fig. 4) is relatively smooth up to ~3.6 eV, where the β values turns to a significant drop. Concomitantly, the sharp, intense rise in the photodestruction spectrum due to the aforementioned $^1\Sigma_u^+$ and/or $^1\Pi_u \leftarrow S_0(^1\Sigma_g^+)$ absorption shows up. Therefore, the dip in the β values around 3.7 eV is suggestive of autodetachment process(es) via these bound excited states embedded in the $D_0(^2\Sigma_u^+) + e^-$ continuum. It would be highly probable that the β values obtained for the $D_1(^2\Sigma_g^+) + e^- \leftarrow S_0(^1\Sigma_g^+)$ channel (squares in

Fig. 4) are also affected by these bound electronic states. The present study has demonstrated that photodestruction action spectroscopy greatly assists the interpretation of energy-dependent LF-PADs.

E. Two-photon detachment via the $S_1(^1\Sigma_u^+)$ state

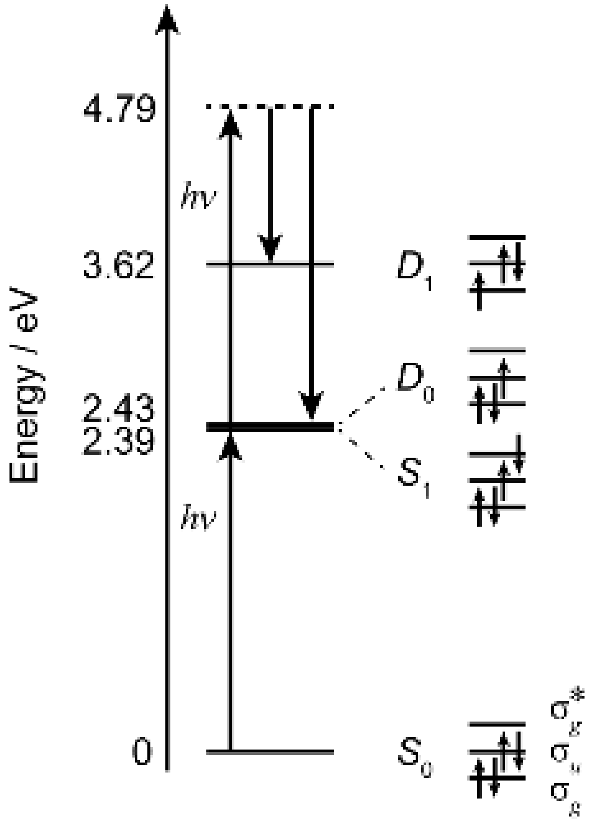

Figure 5. An energy diagram of the two-photon detachment via the $S_1(^1\Sigma_u^+)$ state of Ag_3^-.

By tuning the photon energies at the $S_1(^1\Sigma_u^+) \leftarrow S_0(^1\Sigma_g^+)$ transition, we carried out single-color, two-photon detachment experiments, as schematically illustrated in Fig. 5. Figure 6(a) shows photoelectron spectra obtained with laser pulses at 2.35, 2.39, and 2.43 eV, where the intensity is normalized to unity at the most intense bands in the vicinity of PKE = 0 eV (the original photoelectron images obtained by 2.35- and 2.39-eV irradiation are displayed in Figs. S6(a) and S6(b), respectively, in Supplementary Material). In addition to the intense 0-eV components, the spectrum measured by laser pulses at 2.35 (2.39) eV exhibits two other peaks at 2.22 (2.30) and 1.09 (1.18) eV. Table 1 lists these values along with those expected for two-photon detachment leading to the neutral final states of $D_0(^2\Sigma_u^+)$ and

$D_1(^2\Sigma_g^+)$. Agreement between the peak PKEs observed and those expected confirms that the final states for the higher and the lower energy peaks in Fig. 6(a) are assigned as $D_0(^2\Sigma_u^+)$ and $D_1(^2\Sigma_g^+)$, respectively. As for the 2.43-eV spectrum, the two-photon detachment signals are significantly weaker than the former two cases because the photon energy exceeds the $S_1(^1\Sigma_u^+) \leftarrow S_0(^1\Sigma_g^+)$ resonance energy (see Fig. 4).

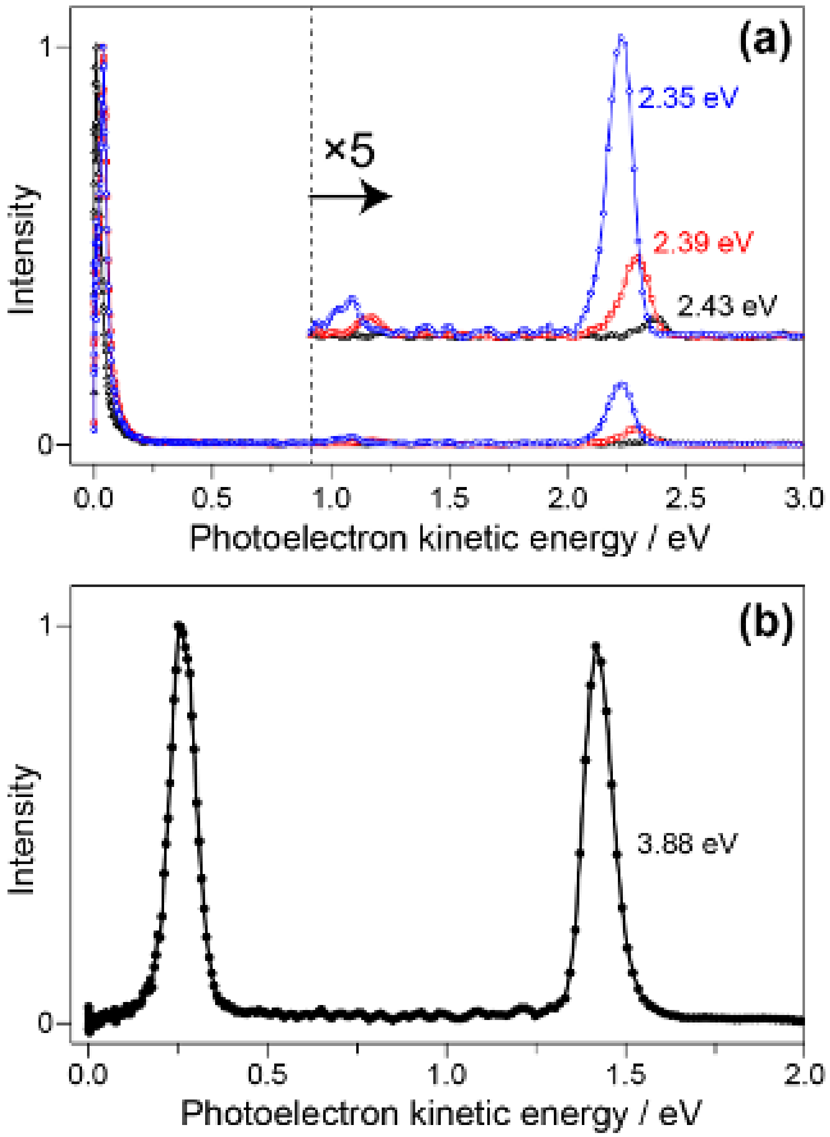

Figure 6. (a) Photoelectron spectra of Ag_3^- obtained by the detachment laser at 2.35 (blue circles), 2.39 (red squares), and 2.43 eV (black triangles). (b) A photoelectron spectrum of Ag_3^- obtained at 3.88 eV. The intensity is in arbitrary units.

First, we discuss the origins of the 0-eV bands. One should note that the 0-eV band profiles of the 2.35- and 2.39-eV spectra are different from that of the 2.43-eV spectrum, as manifested in Fig. S7 in Supplementary Material magnifying the 0-eV bands of Fig. 6(a). These features in the spectral profiles suggest that the 0-eV photoelectrons upon 2.35- and 2.39-eV irradiation are yielded via detachment processes different from that for the 2.43-eV photodetachment case; the latter allows direct one-photon detachment because the photon energy is just at the VDE. Here, one should further note that the 0-eV signals upon 2.35- and 2.39-eV irradiation are generated in a one-photon process as well, as confirmed by the measurement of the laser-power dependence of their intensities (see the inset of Fig. S7), although the photon energy is slightly below the VDE. This odd behavior may be explained as follows: since vibrationally-hot Ag_3^- anions are prepared in our cluster source, one-photon absorption from vibrationally-hot $S_0(^1\Sigma_g^+)$ state into vibrationally-hot $S_1(^1\Sigma_u^+)$ that is energetically above the VDE become possible. Thus, we suppose that the 0-eV components in the 2.35- and 2.39-eV spectra are due to autodetachment from such vibrationally-hot $S_1(^1\Sigma_u^+)$ states into the $D_0(^2\Sigma_u^+) + e^-$ continuum via one-photon processes.

Figure 6(b) shows a photoelectron spectrum obtained by one-photon detachment at 3.88 eV, where two peaks assignable to the $D_0(^2\Sigma_u^+) + e^- \leftarrow S_0(^1\Sigma_g^+)$ and $D_1(^2\Sigma_g^+) + e^- \leftarrow S_0(^1\Sigma_g^+)$ transitions are observed. The intensities of the two peaks are almost comparable, which is in contrast to Fig. 6(a), i.e., two-photon processes. In one-photon detachment, both the transitions are allowed in terms of the frozen-orbital approximation, where only one electron is removed upon photodetachment without altering the configuration of the rest of the electrons (see the electron configurations in Figs. 3 and 5). In two-photon detachment, on the other hand, this approximation readily implies that the $D_0(^2\Sigma_u^+) + e^- \leftarrow S_1(^1\Sigma_u^+) \leftarrow S_0(^1\Sigma_g^+)$ process corresponding to the removal of σ_g^* electron from $S_1(^1\Sigma_u^+)$ is allowed, whereas the $D_1(^2\Sigma_g^+) + e^- \leftarrow S_1(^1\Sigma_u^+) \leftarrow S_0(^1\Sigma_g^+)$ process is forbidden, which requires rearrangement of two electrons upon photodetachment. This accounts for why the $D_1(^2\Sigma_g^+)$ band around 1 eV appears so weakly compared with the $D_0(^2\Sigma_u^+)$ band in Fig. 6(a). Therefore, our experimental result qualitatively supports that the leading electronic configuration of the $S_1(^1\Sigma_u^+)$ state is $(\sigma_g)^2(\sigma_u)^1(\sigma_g^*)^1$ as shown in Fig. 3. Similar arguments were demonstrated in time-resolved photoelectron spectroscopy for isolated molecules,[33,34] where resonantly-enhanced multiphoton ionization via their excited electronic states was employed. Relative intensities of the observed photoelectron signals were discussed by considering the leading electronic configurations of the transient electronic states.

Table 1. Photoelectron kinetic energies expected for two-photon detachment from $S_0(^1\Sigma_g^+)$ to $D_0(^2\Sigma_u^+)$ and $D_1(^2\Sigma_g^+)$ states with 2.35- and 2.39-eV photons along with the observed peak positions in Fig. 6(a).

Two-photon energy / eV	Expected photoelectron kinetic energies / eV[a]		Obsd. peak position / eV
	$D_0(^2\Sigma_u^+)$	$D_1(^2\Sigma_g^+)$	
4.69	2.26	1.07	2.22 / 1.09
4.79	2.36	1.17	2.30 / 1.18

[a] Obtained from the two-photon energies (4.69 or 4.79 eV) and the electron binding energies for the $D_0(^2\Sigma_u^+) + e^- \leftarrow S_0(^1\Sigma_g^+)$ and the $D_1(^2\Sigma_g^+) + e^- \leftarrow S_0(^1\Sigma_g^+)$ transitions (2.43 and 3.62 eV, respectively).

IV. CONCLUSION

We have presented photoelectron imaging spectroscopy of Ag_3^- in the $S_0(^1\Sigma_g^+)$ and $S_1(^1\Sigma_u^+)$ states. Our novel photoelectron imaging apparatus using a 100-kHz tunable fs later system has enabled fast data acquisition of energy dependence of LF-PADs from the outermost two orbitals, σ_u (HOMO) and σ_g (HOMO−1) of Ag_3^-. Highly energy-dependent LF-PAD was obtained for the σ_u orbital in the PKE range of 0 – 1.57 eV. An isotropic LF-PAD ($\beta \sim 0$) was observed at the photodetachment threshold, which exemplifies the Wigner threshold law, whereas the LF-PAD gradually became anisotropic with more photoelectrons perpendicular to the laser polarization (i.e., negative anisotropy) as the PKE increased. The corresponding β parameter exhibited a minimum (–0.4) at 0.46 eV, and thereafter it increased up to ~0.6 at 1.57 eV, with a small dip discernible at 1.2 – 1.3 eV, suggesting autodetachment via bound electronic state(s) embedded in the $D_0(^2\Sigma_u^+)$ + e^- continuum. On the other hand, the photodetachment from the σ_g orbital exhibited a strong positive anisotropy (β ~1) in 0 – 0.39 eV. The simulations of LF-PADs by the ezDyson software qualitatively explained the contrasted trends of the energy-dependent β values, where the photoelectron partial waves with gerade / ungerade symmetries are responsible for the LF-PADs for the σ_u / σ_g orbitals, respectively.

Taking advantage of fs pulses from the 100-kHz tunable light source, we also obtained photoelectron images by two-photon detachment via the $S_1(^1\Sigma_u^+)$ state of Ag_3^-. The relative band intensities for the $D_0(^2\Sigma_u^+)$ and $D_1(^2\Sigma_g^+)$ final states reflected the leading electronic configuration of the transient state, which eventually decays into vibrationally hot $S_0(^1\Sigma_g^+)$ state and/or undergoes Ag–Ag bond dissociation in a finite lifetime. We plan to explore such decay dynamics by applying the present photoelectron imaging spectroscopy to time-resolved measurements.

SUPPLEMENTARY MATERIAL

See the supplementary material for details on acquisition and analysis of photoelectron images, error estimation of anisotropy parameters, and experimental and calculated results that support the discussion of the main text.

ACKNOWLEDGMENTS

This work was supported by Grants-in-Aid for Scientific Research (A) (JP18H03901 and JP22H00317), Scientific Research (B) (JP22H02036 and JP23K23304), and Challenging Research (Exploratory) (JP20K21177 and JP22K19009) from the Japan Society for Promotion of Science (JSPS), the Asahi Glass Foundation, Iketani Science and Technology Foundation, Matsuo Foundation, and

Shimadzu Science Foundation. The authors wish to acknowledge Rin Nomi and Yusuke Okamoto for their experimental assistance.

AUTHOR DECLARATIONS

Conflict of Interest

The authors have no conflicts to disclose.

DATA AVAILABILITY

The data that support the findings of the present study are available on request from the corresponding author, T. H.

AUTHOR CONTRIBUTIONS

Yuta Suzuki: Formal analysis (lead); Investigation (lead); Methodology (supporting); Writing ‑ original draft (equal); Writing ‑ review & editing (equal). **Tasuku Nishizato**: Formal analysis (supporting); Investigation (supporting); Methodology (supporting); Writing ‑ review & editing (equal). **Kazuaki Matsumoto**: Formal analysis (supporting); Investigation (supporting); Methodology (supporting); Writing ‑ review & editing (equal). **Yuta Ushiki**: Formal analysis (supporting); Investigation (supporting); Methodology (supporting); Writing ‑ review & editing (equal). **Yuma Aoki**: Formal analysis (supporting); Investigation (supporting); Writing ‑ review & editing (equal). **Akira Terasaki**: Funding acquisition (equal); Supervision (lead); Writing ‑ review and editing (equal). **Takuya Horio**: Conceptualization (lead); Formal analysis (supporting); Funding acquisition (equal); Investigation (supporting); Methodology (lead); Project administration (lead); Writing ‑ original draft (equal); Writing ‑ review & editing (equal).

REFERENCES

[1] H. Basch, J. Am. Chem. Soc. **103**(16), 4657–4663 (1981).

[2] D.M. Lindsay, L. Chu, Y. Wang, and T.F. George, J. Chem. Phys. **87**(3), 1685–1689 (1987).

[3] C.W. Bauschlicher, S.R. Langhoff, and H. Partridge, J. Chem. Phys. **91**(4), 2412–2419 (1989).

[4] V. Bonačić-Koutecký, L. Češpiva, P. Fantucci, J. Pittner, and J. Koutecký, J. Chem. Phys. **100**(1), 490–506 (1994).

[5] J. Ho, K.M. Ervin, and W.C. Lineberger, J. Chem. Phys. **93**(10), 6987–7002 (1990).

[6] G.F. Gantefor, D.M. Cox, and A. Kaldor, J. Chem. Phys. **93**(11), 8395–8396 (1990).

[7] H. Handschuh, C. Cha, P.S. Bechthold, G. Ganteför, and W. Eberhardt, J. Chem. Phys. **102**(16), 6406–6422 (1995).

[8] S. Wolf, G. Sommerer, S. Rutz, E. Schreiber, T. Leisner, L. Wöste, and R.S. Berry, Phys. Rev. Lett. **74**(21), 4177–4180 (1995).

[9] D.W. Boo, Y. Ozaki, L.H. Andersen, and W.C. Lineberger, J. Phys. Chem. A **101**(36), 6688–6696 (1997).

[10] S. Kawamura, M. Yamaguchi, S. Kono, M. Arakawa, T. Yasuike, T. Horio, and A. Terasaki, J. Phys. Chem. A **127**(29), 6063–6070 (2023).

[11] T. Horio, T. Nishizato, Y. Suzuki, K. Matsumoto, and A. Terasaki, J. Chem. Phys. **162**(2), 026101 (2025).

[12] S. Gozem, A.O. Gunina, T. Ichino, D.L. Osborn, J.F. Stanton, and A.I. Krylov, J. Phys. Chem. Lett. **6**(22), 4532–4540 (2015).

[13] S. Gozem, and A.I. Krylov, WIREs Computational Molecular Science **12**(2), (2022).

[14] T. Horio, K. Minamikawa, T. Nishizato, H. Hashimoto, K. Matsumoto, M. Arakawa, and A. Terasaki, Rev. Sci. Instrum. **93**(8), 083302 (2022).

[15] D.A. Horke, G.M. Roberts, J. Lecointre, and J.R.R. Verlet, Rev. Sci. Instrum. **83**(6), 063101 (2012).

[16] A.T.J.B. Eppink, and D.H. Parker, Rev. Sci. Instrum. **68**(9), 3477–3484 (1997).

[17] K. Minamikawa, T. Nishizato, H. Hashimoto, K. Matsumoto, M. Arakawa, T. Horio, and A. Terasaki, J. Phys. Chem. Lett. **14**(17), 4011–4018 (2023).

[18] Y. Suzuki, K. Matsumoto, R. Nomi, M. Arakawa, T. Horio, and A. Terasaki, J. Phys. Chem. Lett. **15**(16), 4327–4332 (2024).

[19] G.M. Roberts, J.L. Nixon, J. Lecointre, E. Wrede, and J.R.R. Verlet, Rev. Sci. Instrum. **80**(5), 053104 (2009).

[20] E. Epifanovsky, A.T.B. Gilbert, X. Feng, J. Lee, Y. Mao, N. Mardirossian, P. Pokhilko, A.F. White, M.P. Coons, A.L. Dempwolff, Z. Gan, D. Hait, P.R. Horn, L.D. Jacobson, I. Kaliman, J. Kussmann, A.W. Lange, K.U. Lao, D.S. Levine, J. Liu, S.C. McKenzie, A.F. Morrison, K.D. Nanda, F. Plasser, D.R. Rehn, M.L. Vidal, Z.-Q. You, Y. Zhu, B. Alam, B.J. Albrecht, A. Aldossary, E. Alguire, J.H. Andersen, V. Athavale, D. Barton, K. Begam, A. Behn, N. Bellonzi, Y.A. Bernard, E.J. Berquist, H.G.A. Burton, A. Carreras, K. Carter-Fenk, R. Chakraborty, A.D. Chien, K.D. Closser, V. Cofer-Shabica, S. Dasgupta, M. de Wergifosse, J. Deng, M. Diedenhofen, H. Do, S. Ehlert, P.-T. Fang, S. Fatehi, Q. Feng, T. Friedhoff, J. Gayvert, Q. Ge, G. Gidofalvi, M. Goldey, J. Gomes, C.E. González-Espinoza, S. Gulania, A.O. Gunina, M.W.D. Hanson-Heine, P.H.P. Harbach, A. Hauser, M.F. Herbst,

M. Hernández Vera, M. Hodecker, Z.C. Holden, S. Houck, X. Huang, K. Hui, B.C. Huynh, M. Ivanov, Á. Jász, H. Ji, H. Jiang, B. Kaduk, S. Kähler, K. Khistyaev, J. Kim, G. Kis, P. Klunzinger, Z. Koczor-Benda, J.H. Koh, D. Kosenkov, L. Koulias, T. Kowalczyk, C.M. Krauter, K. Kue, A. Kunitsa, T. Kus, I. Ladjánszki, A. Landau, K. V. Lawler, D. Lefrancois, S. Lehtola, R.R. Li, Y.-P. Li, J. Liang, M. Liebenthal, H.-H. Lin, Y.-S. Lin, F. Liu, K.-Y. Liu, M. Loipersberger, A. Luenser, A. Manjanath, P. Manohar, E. Mansoor, S.F. Manzer, S.-P. Mao, A. V. Marenich, T. Markovich, S. Mason, S.A. Maurer, P.F. McLaughlin, M.F.S.J. Menger, J.-M. Mewes, S.A. Mewes, P. Morgante, J.W. Mullinax, K.J. Oosterbaan, G. Paran, A.C. Paul, S.K. Paul, F. Pavošević, Z. Pei, S. Prager, E.I. Proynov, Á. Rák, E. Ramos-Cordoba, B. Rana, A.E. Rask, A. Rettig, R.M. Richard, F. Rob, E. Rossomme, T. Scheele, M. Scheurer, M. Schneider, N. Sergueev, S.M. Sharada, W. Skomorowski, D.W. Small, C.J. Stein, Y.-C. Su, E.J. Sundstrom, Z. Tao, J. Thirman, G.J. Tornai, T. Tsuchimochi, N.M. Tubman, S.P. Veccham, O. Vydrov, J. Wenzel, J. Witte, A. Yamada, K. Yao, S. Yeganeh, S.R. Yost, A. Zech, I.Y. Zhang, X. Zhang, Y. Zhang, D. Zuev, A. Aspuru-Guzik, A.T. Bell, N.A. Besley, K.B. Bravaya, B.R. Brooks, D. Casanova, J.-D. Chai, S. Coriani, C.J. Cramer, G. Cserey, A.E. DePrince, R.A. DiStasio, A. Dreuw, B.D. Dunietz, T.R. Furlani, W.A. Goddard, S. Hammes-Schiffer, T. Head-Gordon, W.J. Hehre, C.-P. Hsu, T.-C. Jagau, Y. Jung, A. Klamt, J. Kong, D.S. Lambrecht, W. Liang, N.J. Mayhall, C.W. McCurdy, J.B. Neaton, C. Ochsenfeld, J.A. Parkhill, R. Peverati, V.A. Rassolov, Y. Shao, L. V. Slipchenko, T. Stauch, R.P. Steele, J.E. Subotnik, A.J.W. Thom, A. Tkatchenko, D.G. Truhlar, T. Van Voorhis, T.A. Wesolowski, K.B. Whaley, H.L. Woodcock, P.M. Zimmerman, S. Faraji, P.M.W. Gill, M. Head-Gordon, J.M. Herbert, and A.I. Krylov, J. Chem. Phys. **155**(8), 084801 (2021).

[21] K.A. Peterson, and C. Puzzarini, Theor. Chem. Acc. **114**(4–5), 283–296 (2005).

[22] B.P. Pritchard, D. Altarawy, B. Didier, T.D. Gibson, and T.L. Windus, J. Chem. Inf. Model **59**(11), 4814–4820 (2019).

[23] J.P. Perdew, Phys. Rev. B **33**(12), 8822–8824 (1986).

[24] A.D. Becke, Phys. Rev. A **38**(6), 3098–3100 (1988).

[25] P.J. Hay, and W.R. Wadt, J. Chem. Phys. **82**(1), 270–283 (1985).

[26] J. Cooper, and R.N. Zare, J. Chem. Phys. **48**(2), 942–943 (1968).

[27] E.P. Wigner, Phys. Rev. **73**(9), 1002–1009 (1948).

[28] R. Mabbs, E.R. Grumbling, K. Pichugin, and A. Sanov, Chem. Soc. Rev. **38**(8), 2169 (2009).

[29] A. Sanov, Annu. Rev. Phys. Chem. **65**(1), 341–363 (2014).

[30] V. Bonačić-Koutecký, P. Fantucci, and J. Koutecký, J. Chem. Phys. **93**(6), 3802–3825 (1990).

[31] C. Bartels, C. Hock, R. Kuhnen, and B. von Issendorff, J. Phys. Chem. A **118**(37), 8270–8276 (2014).

[32] K.M. McHugh, J.G. Eaton, G.H. Lee, H.W. Sarkas, L.H. Kidder, J.T. Snodgrass, M.R. Manaa, and K.H. Bowen, J. Chem. Phys. **91**(6), 3792–3793 (1989).

[33] M. Schmitt, S. Lochbrunner, J.P. Shaffer, J.J. Larsen, M.Z. Zgierski, and A. Stolow, J. Chem. Phys. **114**(3), 1206–1213 (2001).

[34] T. Horio, R. Spesyvtsev, K. Nagashima, R.A. Ingle, Y. Suzuki, and T. Suzuki, J. Chem. Phys. **145**(4), 044306 (2016).